

# Layered Double Hydroxide Nanoparticles/Microparticles (Mg/Al = 2) as Adsorbents for Temperature Swing Adsorption: Effect of Particle Size on CO<sub>2</sub> Gas Evolution Behavior

*Mio Kawashimo<sup>a</sup>, Kaito Matsuda<sup>a</sup>, Ryuta Okumiya<sup>a</sup>, Nana Iio<sup>a</sup>, Ayaka Okuda<sup>a</sup>, Ryota Fukuzaki<sup>a</sup>, Naoki Tarutani<sup>a</sup>, Kiyofumi Katagiri<sup>a</sup>, and Kei Inumaru<sup>a\*</sup>*

<sup>a</sup> Graduate School of Advanced Science and Engineering, Hiroshima University, 1-4-1, Kagamiyama, Higashihiroshima, Hiroshima 739-8527, Japan

Corresponding author: Kei Inumaru, E-mail: inumaru@hiroshima-u.ac.jp

KEYWORDS: layered structure, CO<sub>2</sub> adsorbent, carbonate ion, intercalation, structural transformation, temperature swing adsorption

## ABSTRACT

Mg–Al layered double hydroxide (LDH, Mg/Al  $\approx$  2) nanoparticles/microparticles with systematically controlled sizes were prepared using a hydrothermal method, and their performance as CO<sub>2</sub> adsorbents for temperature swing adsorption (TSA) cycling was investigated. During continuous heating, gas evolution occurred over three distinct steps for all samples. During the second step of the multistep structural transformations (i.e. partial dehydroxylation of the layers followed by the coordination of carbonate ions to the metal ions), relatively large amounts of CO<sub>2</sub> were evolved without the collapse of the layered crystal structure, whereas most of the interlayer CO<sub>3</sub><sup>2-</sup> ions were retained in the interlayer spaces. The amount of CO<sub>2</sub> evolution increased as the particle size decreased. Subsequently, the amount of CO<sub>2</sub> desorption was measured over repeated TSA cycles in the temperature range of 463–603 K. All samples exhibited considerable CO<sub>2</sub> desorption capacities, wherein water vapor enhanced the performance. *In situ* Fourier transform infrared spectroscopy revealed that the adsorption/desorption cycles were almost reversible. A slight change in the interlayer distance detected by *in situ* X-ray diffraction suggested that the insertion and removal of some carbonate species partly occurred in the interlayer spaces of the LDHs. The present study indicates the potential of LDH nanoparticles/microparticles for TSA adsorbents.

## INTRODUCTION

Layered double hydroxides (LDHs) are well-known materials;<sup>1</sup> however, they have recently attracted growing attention owing to their wide variety of advanced functions. For example, LDHs have been applied in solid-base catalysts for organic reactions,<sup>2–4</sup> photocatalysts for CO<sub>2</sub> reduction,<sup>5,6</sup> ion storage materials,<sup>7</sup> capacitors,<sup>8</sup> and electrode catalysts for water splitting,<sup>9,10</sup> which are important research fields in the contexts of green chemistry and sustainable energy. Layered nickel hydroxides and Fe-containing LDHs were found to be highly promising electrode catalysts for water oxidation.<sup>9,10</sup>

LDHs possess the general formula  $M^{2+}_{1-x}M^{3+}_x(\text{OH})_2 A^{n-}_{x/n} \cdot m\text{H}_2\text{O}$ , wherein the positive charge density of the metal hydroxide layer is determined by the  $M^{2+}/M^{3+}$  ratio, and  $n$ -valent  $A^{n-}$  anions are inserted in the interlayer spaces to neutralize the positive charge. Various metal ions can be used to form LDHs. Specifically,  $M^{2+}$  represents a divalent cation, such as  $\text{Mg}^{2+}$ ,  $\text{Ni}^{2+}$ , or  $\text{Zn}^{2+}$ , while  $M^{3+}$  represents a trivalent cation, such as  $\text{Al}^{3+}$ ,  $\text{Ga}^{3+}$ ,  $\text{Fe}^{3+}$ , or a transition-metal ion. Similarly, many types of anions can be used as the interlayer anions of LDHs, such as  $\text{CO}_3^{2-}$ ,  $\text{NO}_3^-$ , and  $\text{Cl}^-$ .<sup>1</sup>

Mg–Al LDHs, which contain  $\text{Mg}^{2+}$  and  $\text{Al}^{3+}$  ions as the divalent and trivalent cations, respectively, are known to have a strong affinity for gaseous CO<sub>2</sub>; thus, they are considered promising CO<sub>2</sub> adsorbents.<sup>1, 11–13</sup> Specifically, ambient CO<sub>2</sub> is readily absorbed into LDHs, forming  $\text{CO}_3^{2-}$  interlayer anions. Many researchers have reported multistep structural transformation and gas evolution from Mg–Al LDHs.<sup>14–23</sup> It has been reported that the evolution of gaseous CO<sub>2</sub> from Mg–Al LDHs is accompanied by the collapse of the layered crystal structure at high temperatures.<sup>14–16</sup> In this context, the Mg–Al LDH has been studied in detail to obtain information regarding its crystal chemistry and potential applications. The crystal

chemistry of this LDH is particularly attractive owing to its “memory effect,” wherein the layered crystal structure decomposes at temperatures of  $>650$  K to evolve  $\text{CO}_2$  and water vapor and generate a Mg–Al mixed oxide with a rock-salt structure. This oxide readily reproduces the layered structure of LDH in the presence of water at an ambient temperature, giving the impression that it remembers the original structure. However, the mechanism responsible for this “memory effect” remains controversial.<sup>24,25</sup>

In a previous study,<sup>26</sup> our group provided a clear description of the structural transformation steps occurring in a well-crystallized Mg–Al LDH sample with an Mg/Al atomic ratio of 2:1. We also presented the comprehensive analysis of the chemical and structural transformations of Mg–Al LDH particles with different Mg/Al ratios.<sup>27</sup> These transformations involve three steps: (1) the release of interlayer water; (2) partial dehydroxylation of the hydroxide layers accompanied by the formation of coordinatively unsaturated sites and the coordination of carbonate ions to the metal centers; and (3) collapse of the layered structure accompanied by complete dehydroxylation of the layers and decomposition of the interlayer  $\text{CO}_3^{2-}$  at relatively high temperatures. These studies indicated that stepwise dehydroxylation is not ascribable to the different coordination environments of the hydroxyl groups.<sup>26</sup> The reason is possibly that the structure after the partial dehydroxylation of the metal hydroxide layers is relatively stable. We provide a molecular/atomic-level picture of the structure during each transformation step. Experimental data indicated that step (1) significantly reduces the interlayer distance of the LDH from  $\sim 7.6$  to  $\sim 6.7$  Å (a reduction of  $\sim 0.9$  Å); the structurally optimized model obtained via first-principles density functional theory (DFT) calculations indicated that this reduction was likely due to waving of the metal hydroxide layers in the crystal structure.<sup>27</sup> The differences in the chemical/structural transformations of the Mg–Al LDHs with Mg/Al = 2 and 3 appear to be

significant: the former exhibits a distinct three-step transformation (steps (1)–(3)), whereas the latter exhibits an apparent two-step transformation. However, the transformations essentially consist of three steps for both cases. The difference in the temperature range of step (2) causes the apparent difference.<sup>27</sup>

Thus, we herein describe the preparation of Mg–Al LDH (Mg/Al  $\approx$  2) nanoparticles/microparticles with systematically controlled particle sizes via hydrothermal synthesis without the use of organic reagents, followed by an evaluation of their performance as a CO<sub>2</sub> adsorbent for temperature swing adsorption (TSA). In recent studies, researchers developed synthesis methods for nanoparticles<sup>28–31</sup> and nanosheets<sup>32</sup> of LDHs. However, most of them use organic molecules to control the particle sizes, and the molecules adsorbed on the particle surfaces sometimes interfere with surface functions such as catalysis. Then, the gas evolution behaviors of samples with different particle sizes (<100 nm = nanoparticles,<sup>33</sup> larger sizes = microparticles) were measured quantitatively during continuous heating. According to the IUPAC recommendation,<sup>33</sup> some samples were categorized as nanoparticles because their sizes were <100 nm. Additionally, the CO<sub>2</sub> desorption performance of the prepared samples was measured over repeated TSA cycles in the temperature range of 363–603 K, and the effect of water vapor was examined. Furthermore, *in situ* Fourier transform infrared adsorption spectroscopy (FT-IR) and *in situ* X-ray powder diffraction (XRD) experiments are used to elucidate the detailed behavior of the adsorbed species and the adsorbents during the adsorption and desorption processes. This study highlights the potential performance of Mg–Al LDH (Mg/Al  $\approx$  2) nanoparticles/microparticles as TSA adsorbents.

## EXPERIMENTAL METHODS

### Synthesis of Mg–Al LDH Samples

The Mg–Al LDH particles were synthesized using a hydrothermal method<sup>34–36</sup> over various heating periods. For this purpose, an Na<sub>2</sub>CO<sub>3</sub> solution (0.026 M, 120 cm<sup>3</sup>) and an NaOH solution (0.3 M, 120 cm<sup>3</sup>) were mixed to obtain a carbonate solution. Separately, an MgCl<sub>2</sub> solution (0.6 M, 30 cm<sup>3</sup>) was mixed with an AlCl<sub>3</sub> solution (0.2 M, 30 cm<sup>3</sup>) to obtain a Mg and Al mixed solution. This solution was rapidly added to the carbonate solution under stirring. After stirring for 10 min at room temperature, a white solid precipitated, and the pH of the suspension reached ~9. This suspension was subsequently divided into 12 centrifuge tubes (50 cm<sup>3</sup> each) and centrifugally separated at  $9390 \times g$  for 2 min. After removal of the supernatant, deionized water (20 cm<sup>3</sup>) was added to each tube, and the suspensions were mixed using a vortex mixer to disperse the white precipitates. This washing procedure was performed three times for each tube. The solutions in the tubes were then transferred to six autoclaves (45 cm<sup>3</sup>) and hydrothermally treated at 373 K. To obtain four samples with different particle sizes, hydrothermal treatment for the set of six autoclaves was performed for durations of 1, 4, 16, and 72 h. After the autoclaves were cooled to room temperature, the supernatant was removed via ultracentrifugation at  $18510 \times g$  for 30 min. The white precipitate was then dried in vacuum conditions at room temperature to obtain Mg–Al LDH powder. The samples were denoted as LDH[1h], LDH[4h], LDH[16h], and LDH[72h], wherein the thermal treatment time is shown in the square brackets. The Mg/Al ratios of the samples were determined using inductively coupled plasma atomic emission spectroscopy (ICP-AES).

## Characterization and Analysis of Thermal Decomposition Behaviors of LDH Samples

The *ex-situ* XRD patterns of the samples were measured using a D8 ADVANCE diffractometer with Cu K $\alpha$  radiation. The evolution rates of gaseous H<sub>2</sub>O and CO<sub>2</sub> from the LDH samples upon heating were measured using a gas-flow system equipped with a Q-mass spectrometer. The LDH sample (30 mg) was set in a quartz tube reactor and heated to 1073 K at a temperature ramp rate of 10 K min<sup>-1</sup> under a flow of Ar (100 cm<sup>3</sup> min<sup>-1</sup>). The outlet gas was analyzed using a quadrupole mass (Q-mass) spectrometer (CO<sub>2</sub>,  $m/z$  = 44; H<sub>2</sub>O,  $m/z$  = 18). The advantage of our experiment is that the absolute CO<sub>2</sub> evolution rate could be determined following the calibration of the apparatus using a standard gas. As H<sub>2</sub>O molecules are readily adsorbed onto the inner walls of the apparatus, the Q-mass signal intensity does not reflect the precise evolution rate of H<sub>2</sub>O. Therefore, the Q-mass intensity ( $m/z$  = 18) was used as the relative H<sub>2</sub>O evolution rate. Variable temperature powder XRD measurements (*in situ* XRD) were performed under vacuum conditions using a D8 Advance diffractometer (Bruker) equipped with an *in situ* sample chamber (Anton-Paar TTK-450). Scanning electron microscopy (SEM) images of the samples were taken with a Hitachi S-4800. The particle size distributions were measured via dynamic laser scattering (DLS). The data were recorded and analyzed with an Otsuka Electric ELS-Z. N<sub>2</sub> adsorption isotherms were measured at 77 K with a BELSorp Mini (MicrotracBEL).

## Repeated Temperature Swing Adsorption/Desorption Experiments

Two sets of conditions were adopted in the repeated TSA experiments: “dry” and “wet” conditions. All the experiments were conducted using a gas-flow system with a Q-mass spectrometer. In each case, the fresh LDH sample was set in the reactor and heated to 493 K

under a flow of Ar ( $100\text{ cm}^3\text{ min}^{-1}$ ). After this temperature was maintained for 15 min, the sample was heated to 603 K at a temperature ramp rate of  $10\text{ K min}^{-1}$  under a flow of Ar ( $100\text{ cm}^3\text{ min}^{-1}$ ). The outlet gas was analyzed using a Q-mass spectrometer ( $\text{CO}_2$ ,  $m/z = 44$ ;  $\text{H}_2\text{O}$ ,  $m/z = 18$ ). This gas analysis step was designated as the initial step. After the temperature of 603 K was maintained for 15 min, the samples were cooled to 463 K. For the subsequent  $\text{CO}_2$  adsorption procedure, either dry or wet conditions were employed. For the dry conditions, the sample was exposed to a  $\text{CO}_2$  flow ( $100\text{ cm}^3\text{ min}^{-1}$ ) at 463 K for 1 h without adding  $\text{H}_2\text{O}$ . In contrast, for the wet conditions, water vapor (35.5 kPa) was added to the  $\text{CO}_2$  flow. All the samples were then heated to 603 K under a dry Ar flow at a rate of  $10\text{ K min}^{-1}$ . The outlet gas was analyzed during this desorption step (cycle 1). The aforementioned  $\text{CO}_2$  adsorption/desorption steps were repeated for both conditions to obtain the data corresponding to cycles 2, 3, etc. The  $\text{CO}_2$  desorption amounts were calculated by integrating the calibrated Q-mass signal ( $m/z = 44$ ) data.

### ***In situ* FT-IR and *in situ* XRD experiments**

*In situ* FT-IR measurements were performed using an FT-IR 4200 spectrometer (JASCO) combined with a glass cell connected to a vacuum system with gas/vapor inlets. A small amount of sample powder was dispersed in a small amount of deionized water. The resulting dispersion was applied to a Si single-crystal substrate and dried in an ambient atmosphere to form a thin film of the sample on the substrate. This thin film/substrate sample was placed in a glass *in situ* cell, and the spectra were measured in the transmission mode. The cell contained a heated zone with a controlled temperature, and it was possible to move the sample between the heated zone and measurement position under a controlled atmosphere or vacuum conditions. Because the cell



was not heated around the measurement position, the maximum pressure of the H<sub>2</sub>O vapor introduced into the cell was restricted to less than the saturated vapor pressure at room temperature to avoid condensation of liquid water.

To reproduce the dry TSA conditions, a series of *in situ* FT-IR experiments were conducted. A fresh sample was heated *in vacuo* at 463 and 603 K. Subsequently, the samples was exposed to 80 kPa of CO<sub>2</sub> at 463 K (the spectrum recorded here was designated as CO<sub>2</sub>-ads1). The sample was then evacuated at 603 K (CO<sub>2</sub>-des1), and these procedures were repeated to obtain the data for CO<sub>2</sub>-ads2, CO<sub>2</sub>-des2, etc. *In situ* XRD measurements were also conducted under these simulated dry conditions.

When attempting to reproduce the wet conditions, the experimental procedures were complex because of the limitations regarding the H<sub>2</sub>O vapor pressure (the *in situ* FT-IR and XRD cells were restricted to room temperature, and only the sample zones could be heated). Thus, a fresh sample was evacuated at room temperature and then at 463 K. Similar to our previous study,<sup>27</sup> only part of the interlayer water was removed at 463 K. A considerable amount of water remained in the interlayer spaces (LDH with Mg/Al = 2:1). After the spectrum was obtained at this temperature, the sample was evacuated at 603 K. At this temperature, the interlayer water molecules were eliminated, and partial dehydroxylation of the hydroxyl layers occurred, followed by coordination of the carbonate ions to the metal ions (step (2)). The spectrum was measured (603 K), and the sample was exposed to 2 kPa of H<sub>2</sub>O vapor at room temperature. After subsequent evacuation at room temperature for 30 min, another spectrum was recorded (denoted as H<sub>2</sub>O-ads), and the sample was heated to 463 K under vacuum. The samples were then exposed to 80 kPa of gaseous CO<sub>2</sub> for 15 min and evacuated. The spectrum recorded at this point was denoted as CO<sub>2</sub>-ads. Finally, the sample temperature was increased to 603 K under

vacuum, and the spectrum was measured (denoted as CO<sub>2</sub>-des). All the *in situ* XRD measurements were conducted under a controlled atmosphere, similar to the aforementioned FT-IR experiments.

### **Structural Optimization and Infrared Absorption Simulation of Models for Hydroxide Layer and Adsorbed Species by DFT Calculations**

The structural models of the hydroxide layer slabs were created using the software package Materials Studio Visualizer (BIOVIA), and their structures were optimized by CASTEP 2021. The unit cells of the periodic structural models contained one layer slab of metal hydroxides of the LDHs. The structure of the layer was extracted from the reported single-crystal experimental data.<sup>15</sup> The interlayer distance was set as approximately 23 Å to eliminate interactions between the layers. The interlayer anions were omitted, and appropriate charges were assumed for the calculations, depending on the model and adsorbed species assumed. Dehydroxylated metal hydroxide layer models were created by removing a pair of a hydroxyl (OH<sup>-</sup>) group and a proton (H<sup>+</sup>) from each of the models. When adsorbed species were considered, a CO<sub>2</sub> molecule, CO<sub>3</sub><sup>2-</sup> anion, or CO<sub>2</sub> molecule with an O<sup>2-</sup> anion was placed on the slab model, and then structural optimization was performed via first-principles DFT calculations (CASTEP 2021). The structural optimization of the models was performed with fixed cell parameters. No symmetry was assumed (*P1*), and all atoms were set to be mobile. In the structural optimization, the plane wave basis set cutoff was set as 630 eV. To simulate the infrared (IR) spectra of the models, linear response or density functional perturbation theory<sup>37,38</sup> was used as it is implemented in CASTEP 2021. One CO<sub>3</sub><sup>2-</sup> ion, two Mg<sup>2+</sup> ions and one Al<sup>3+</sup> ion were set to be mobile in the optimized models. In the calculation, a 3 × 3 × 1 Monkhorst–Pack grid was employed, and the

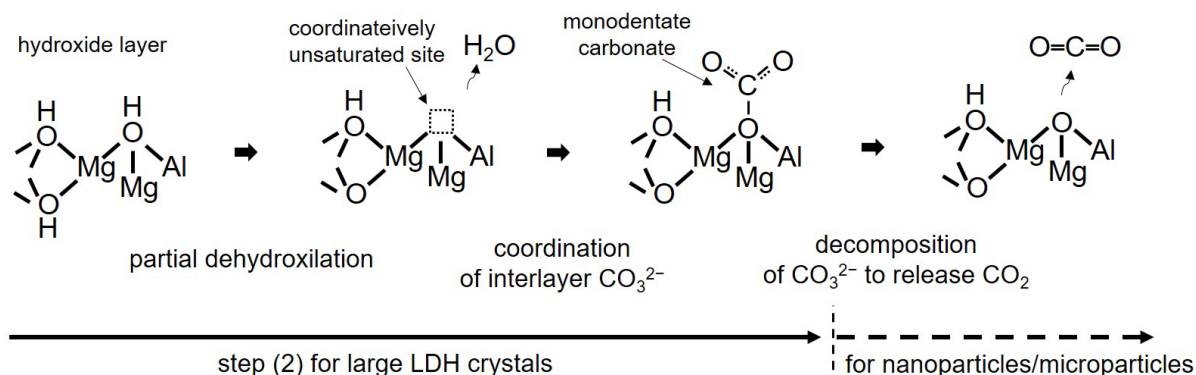
plane wave basis set cutoff was set as 990.0 eV. Norm conserving pseudopotentials, the generalized gradient approximation, the PBESolid functional, and the TS method for DFT-D correction were used, as implemented in CASTEP 2021.

## RESULTS AND DISCUSSION

### Preliminary First-Principles DFT Calculations for Possible Structural Models of Adsorbed Species and Their Infrared Absorption Spectra

As for surface functional materials such as heterogeneous catalysts and adsorbents, the use of crystalline materials is advantageous to understand and design the functions at the molecular level, because plausible surface structural models can be constructed on the basis of their bulk crystal structures.<sup>39</sup> In the case of LDHs, the hydroxide layer slab can be used as a reliable surface model of the adsorbents. In previous studies,<sup>26,27</sup> we proved that drastic chemical and structural transformation of Mg–Al LDH (Mg/Al = 2) occurs at an intermediate temperature

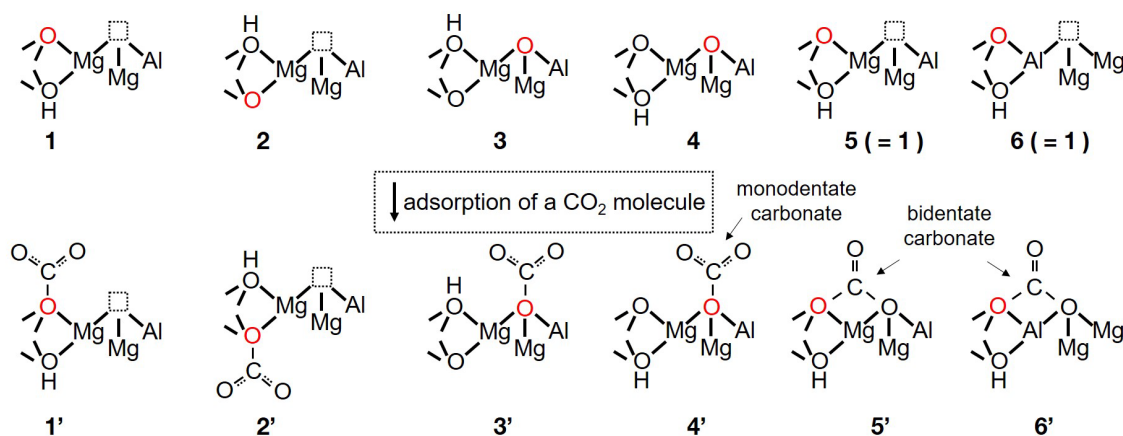
Scheme 1. Transformation of the hydroxide layer at an elevated temperature (~580 K, step (2)).



range (~580 K, as the second step in the three-step transformation). A schematic of the transformation reactions is presented in Scheme 1. Here, the metal hydroxide layers are partially dehydroxylated to form coordinatively unsaturated sites, followed by the coordination of the interlayer  $\text{CO}_3^{2-}$  ions to the metal ions to form monodentate carbonate species. In the case of microparticle samples, large amounts of  $\text{CO}_2$  evolution were observed from the LDH in same temperature range.<sup>27</sup> The  $\text{CO}_2$  evolution likely originated from  $\text{CO}_3^{2-}$  ions (the final step in Scheme 1) on the outer surfaces of the particles and/or in the interlayer spaces in the peripheral part of the plate-like LDH particles, whereas most of  $\text{CO}_3^{2-}$  ions are retained in the interlayer spaces.

The chemical interactions between  $\text{CO}_2$  molecules and the surface sites are important for designing  $\text{CO}_2$  adsorbents. When chemical adsorption of  $\text{CO}_2$  molecules occurs on the surfaces of metal oxides, they interact with surface oxide ions to form carbonate species. One  $\text{CO}_2$

Scheme 2. Possible structures of adsorption sites (upper models) and adsorbed species (lower models).



molecule requires one  $\text{O}^{2-}$  ion to form a carbonate species on the surfaces. Scheme 2 shows possible structural models of the surface adsorption sites and of corresponding adsorbed species on an Mg–Al LDH hydroxide layer.  $\text{CO}_2$  molecules interact with the surface oxygen ions highlighted in red to form carbonate adsorbed species, as shown in Scheme 2. The models of the adsorption sites in Scheme 2 (upper models) are developed considering the reactions in Scheme 1. After the partial dehydroxylation, the oxygen ion from which  $\text{H}^+$  has been removed is exposed to the surfaces as a naked  $\text{O}^{2-}$  ion (the first step in Scheme 1). Furthermore, one  $\text{O}^{2-}$  ion is left on the surface after the decomposition of one carbonate ion (the final step in Scheme 1). Thus, at least two types of surface oxygen ions with different chemical environments are candidate adsorption sites for  $\text{CO}_2$  molecules. The hydroxide layers before dehydroxylation may be inert as  $\text{CO}_2$  adsorbents because the surfaces fully covered with hydroxide ions have no sites to interact with  $\text{CO}_2$  molecules. In Scheme 2, surface site models **1** and **2** are introduced considering the dehydroxylation reaction. Models **3** and **4** correspond to the results of the decomposition of the carbonate species. Models **5** and **6** are equivalent to model **1**. Here, there are two options in the dehydroxylation reaction: the  $\text{H}^+$  and  $\text{OH}^-$  are removed from the same side of the hydroxide layer (models **1**, **4**, **5**, and **6**) or removed from the front and back sides (models **2** and **3**). Thus, the models of adsorbed species **1'–6'** corresponding to models **1–6** are considered (Scheme 2).

Next, we constructed slab models for theoretical calculations. The unit cell ( $a = b = 5.28 \text{ \AA}$ ,  $c = 22.8 \text{ \AA}$ , space group  $P1$ ) of each model contained one layer slab, and the content of the unit cell was  $\text{Mg}_2\text{Al}(\text{OH})_2$  before dehydroxylation. Then,  $\text{H}^+$  and  $\text{OH}^-$  were removed from appropriate positions to form the initial models of **1** and **2** in Scheme 2. To obtain the initial structures for **1'** or **2'**, a C atom and two O atoms were placed into the model such that the atoms exactly reproduced the bond lengths and bond angles of carbonate ions optimized in an LDH structural

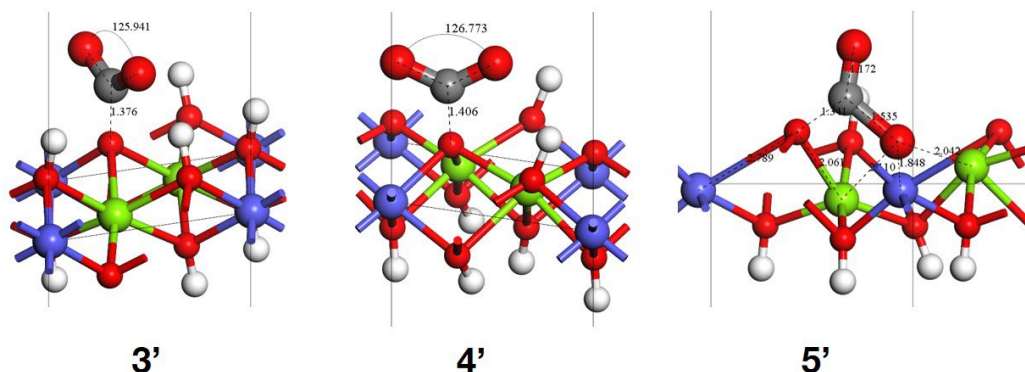


**Figure 1.** Candidates for the adsorbed species structures successfully optimized via first-principles DFT calculations. Mg, green; Al, blue; O, red; C, grey; H, white.

model in our previous study.<sup>26</sup> Then, structural optimization was performed for each of the obtained initial models. If the carbonate species in the models are stable, the structures are likely to converge to optimized structures similar to the initial models. However, for **1'** and **2'**, the calculation reached a structure consisting of the surface site (**1** or **2**) and a linear  $\text{CO}_2$  molecule located at a distance of up to  $>2.5 \text{ \AA}$  from the surface site. Scheme S1 in the Supporting Information (SI) summarizes these results. Thus, the present calculations failed to obtain optimized structures corresponding to **1'** and **2'**.

However, the optimized structures corresponding to **3'**, **4'**, **5'**, and **6'** were successfully obtained. These structures are shown in Figure 1. In the optimized structure **3'** or **4'**, the CO<sub>2</sub> molecule bends, with a bond angle of approximately 126°, and the distance from surface O<sup>2-</sup> to C atom is as short as 1.4 Å, indicating that the CO<sub>2</sub> molecule forms a chemical bond with the surface O<sup>2-</sup> to produce monodentate carbonate species. Here, each of their initial structures consists of the surface site model (**3** or **4**) and a linear CO<sub>2</sub> molecule at a distance of up to 2 Å, as shown in Scheme S1 in the SI. In structure **5'**, the bidentate carbonate species is coordinated to one Mg<sup>2+</sup> ion. We also obtained another bidentate model, i.e., **6'**, in which the carbonate species is coordinated to one Al<sup>3+</sup> ion. To obtain the optimized models **5'** and **6'** with bidentate

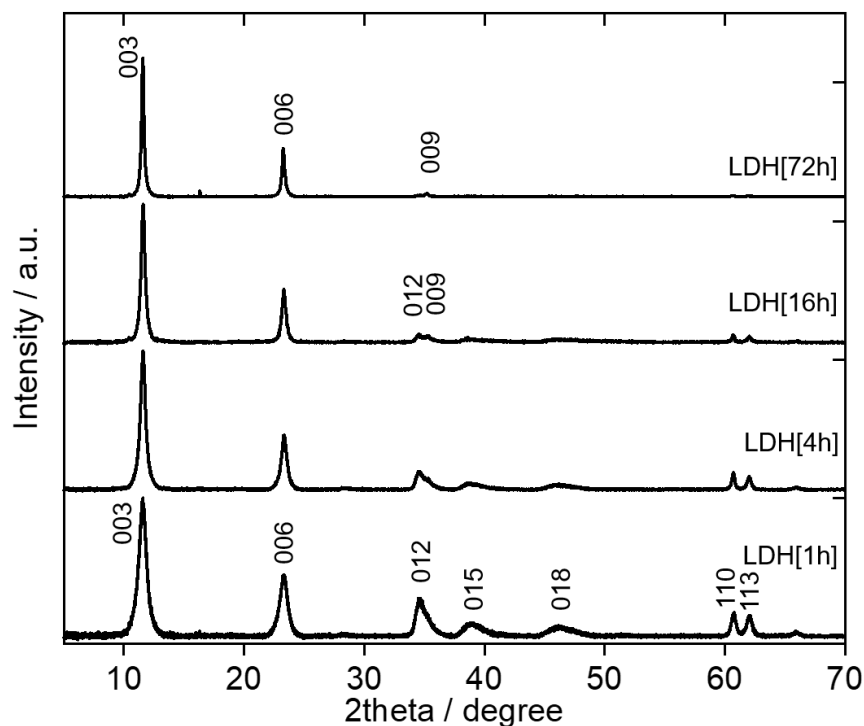


**Figure 2** XRD patterns of the Mg–Al LDH (Mg/Al  $\approx$  2) samples with interlayer CO<sub>3</sub><sup>2-</sup> anions prepared via hydrothermal synthesis. In the sample names, the durations of the hydrothermal treatments are shown in parentheses.

structures, we set their initial structures to the bidentate form, as shown in Scheme S1 (SI).

To obtain more information from the calculation, IR absorption spectra were calculated on the basis of the structural models. The calculated absorption wavenumbers for the carbonate species are presented in Table S1. The monodentate species (**3'** and **4'**) exhibited two absorption bands,

Table 1. Properties of the Mg–Al LDH nanoparticles/microparticles prepared via hydrothermal synthesis.

sample	crystal thickness	DLS results		SEM results		$S_{\text{BET}}$  /m <sup>2</sup> g <sup>−1</sup>	$S_{\text{side}}$  / $S_{\text{BET}}$
	along [001] <sup>a</sup>	$d_{\text{DLS}}^b$	poly- dispersity index	$d_{\text{SEM}}^b$	$S_{\text{side}}^c$		
	$L$ /nm	/nm		/nm	/m <sup>2</sup> g <sup>−1</sup>		
LDH[1h]	10.8	46.6	0.221	43.0	22.4	154.9	0.145
LDH[4h]	15.6	64.5	0.159	71.0	13.8	88.5	0.156
LDH[16h]	20.1	88.6	0.154	82.9	11.4	79.3	0.143
LDH[72h]	31.8	106.8	0.143	116.2	8.6	59.7	0.144

<sup>a</sup>Crystal thickness along the [001] direction calculated from the FWHM of the 003 diffraction peaks. <sup>b</sup>Mean particle diameter determined from the DLS data or the SEM images. <sup>c</sup>Total surface areas of the side surfaces of the plate-like particles calculated from the SEM images (distributed diameters) and the crystal densities. See the text for the detailed calculation method.



which were close together, and their split widths were  $<300\text{ cm}^{-1}$ , whereas the bidentate models (**5'** and **6'**) exhibited larger split widths, which was consistent with previously reported experimental data for metal complex compounds.<sup>40</sup> The data presented in the bottom row of Table S1 correspond to monodentate carbonate forming hydrogen bonds with hydroxyl groups on both hydroxide layers (floor and ceiling) of the interlayer spaces (see the SI of our previous paper<sup>26</sup>). It is likely that hydrogen bonding also affects the split width of the two signals. In fact, the models used here are small; thus, a possible question to raise is how much the neighboring unit cells affect the above results. Providing a complete answer to this question is beyond the scope of the preliminary calculation. We checked whether the surface carbonate species similar to model **3'** in Figure 1 was obtained in a model with a far larger unit cell via structural optimization. Here, the cell was 12 times larger than that of model **3'**. It was confirmed that a monodentate carbonate species was obtained in the model with a far larger unit cell, as shown in Scheme S2 (SI). The values such as IR band wavenumbers obtained from the calculations provide guidance, although they are preliminary results and may contain errors.

### Characterization of LDH Samples

Figure 2 shows the XRD patterns recorded for the Mg–Al LDH nanoparticles/microparticle samples prepared using different hydrothermal treatment times. The lattice parameters determined from the diffraction peak positions are presented in Table S1 in the SI. The diffraction patterns were similar to those previously reported for Mg–Al LDHs.<sup>1</sup> Notably, as the hydrothermal treatment time was increased, the diffraction peaks of 003 and 006 became sharper. Thus, the crystallite thicknesses were calculated from the full widths at half maximum (FWHMs) of the 003 diffraction peaks using the Scherrer equation (Table 1), indicating that increasing the

hydrothermal treatment time increased the crystal thickness in the direction perpendicular to the basal plane of the layered crystal structure. For LDH[16h] and LDH[72h], the diffraction peaks of all crystal planes except those parallel to the hydroxide layers were relatively weak owing to the preferred orientation of the plate-like LDH crystallites in the powder samples.

The SEM images recorded for the Mg–Al LDH samples are shown in Figure 3. In the case of the LDH[1h] specimen (Figure 3a), hexagonal plate-like crystallites with diameters of several tens of nanometers were observed, although a small number of crystallites had diameters of >50 nm. For the LDH[4h] sample, most crystallites had diameters of 30–80 nm. Therefore, these two

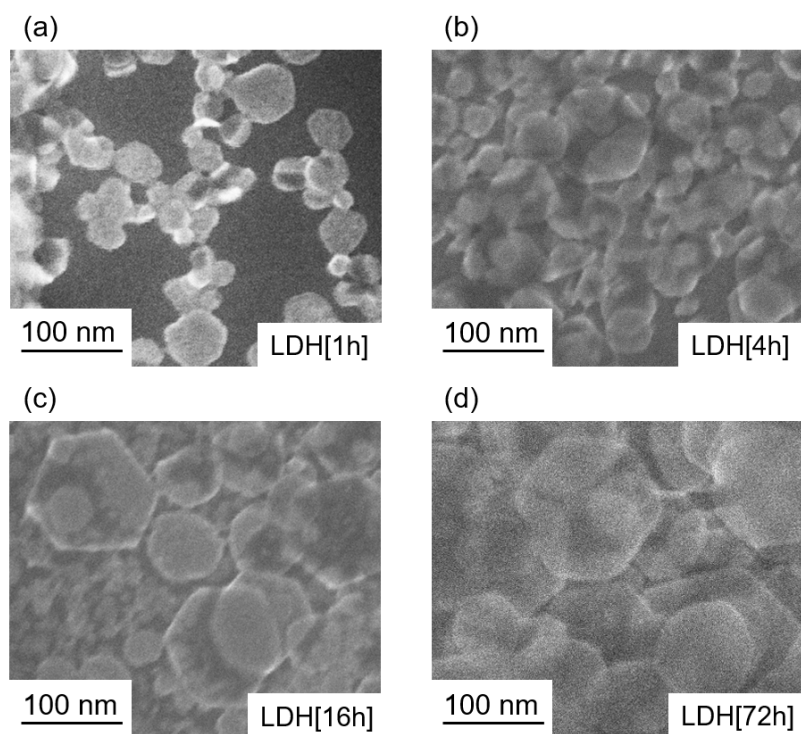


**Figure 3.** SEM images of the Mg–Al LDH ( $\text{Mg}/\text{Al} \approx 2:1$ ) samples: (a) LDH[1h], (b) LDH[4h], (c) LDH[16h], and (d) LDH[72h].

samples were categorized as nanoparticles, as their particle diameters were  $<100$  nm.<sup>33</sup> As indicated by the SEM image in Figure 3c, the LDH[16h] sample contained large plate-like crystallites with sizes of  $>100$  nm, although smaller particles were also observed. When the hydrothermal treatment time was increased to 72 h, the sample contained well-developed plate-like crystallites (Figure 3d) reaching sizes of 100–200 nm. Therefore, the XRD and SEM results indicated that longer hydrothermal treatment durations resulted in larger LDH crystallites.

This trend was confirmed by measuring the particle size distributions of the various specimens using DLS, as shown in Figure 4 and Table 1. In addition, the nitrogen adsorption isotherms

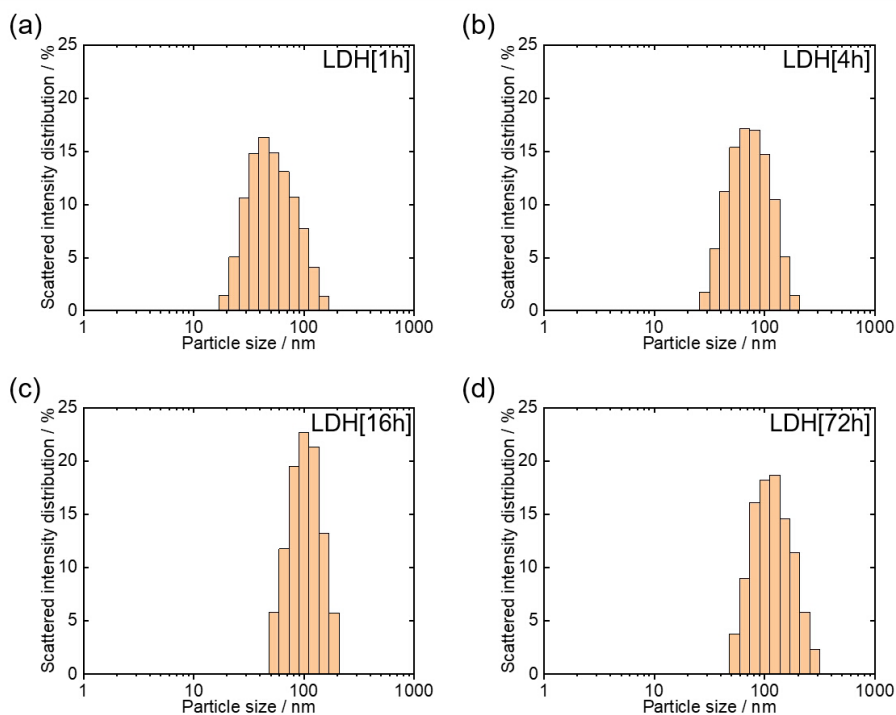


**Figure 4.** Particle size distributions of the Mg–Al LDH samples ( $\text{Mg}/\text{Al} \approx 2:1$ ) obtained via DLS: (a) LDH[1h], (b) LDH[4h], (c) LDH[16h], and (d) LDH[72h].

were measured at 77 K (see Figure S1). The derived Brunauer–Emmett–Teller (BET) surface areas ( $S_{\text{BET}}$ ) are presented in Table 1. Figure 4 clearly shows that the crystallite size increased with the hydrothermal treatment time; the average diameter of the LDH[1h] specimens was 46.6 nm, and that of the LDH[72h] particles reached 106.8 nm. Accordingly, the BET surface area decreased from 154.9 to 59.7 m<sup>2</sup> g<sup>-1</sup> in the order of LDH[1h], LDH[4h], LDH[16h], and LDH[72h]. These results indicate that the size of the LDH particles can be controlled by altering the hydrothermal treatment time.

### Gas Evolution Behaviors of LDH Samples during Continuous Heating

To evaluate the potential performance of these LDH samples as CO<sub>2</sub> adsorbents, their gas

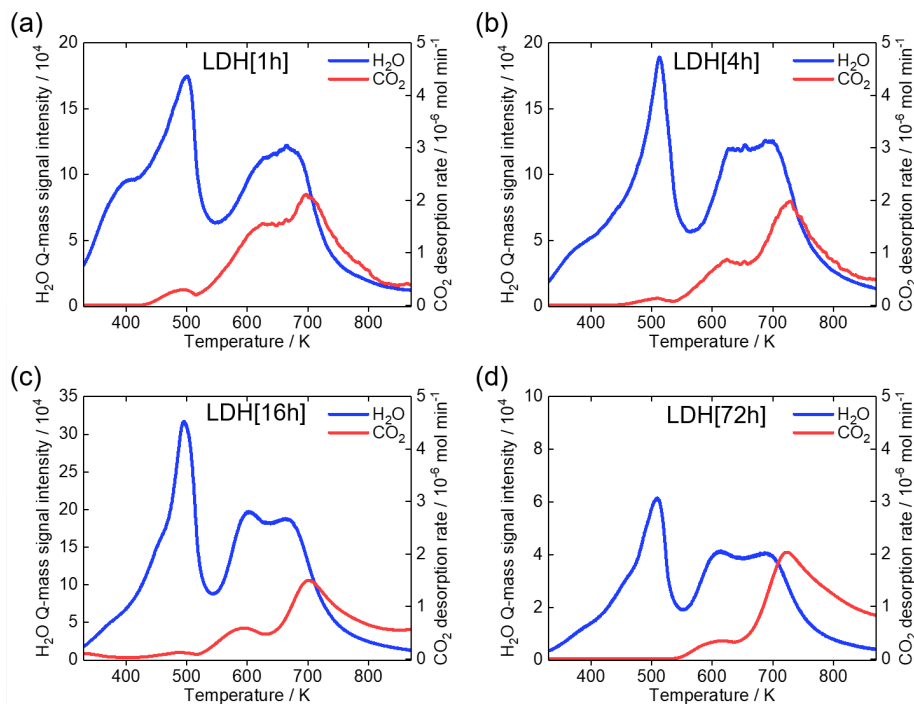


**Figure 5.** Evolution rates of gaseous H<sub>2</sub>O and CO<sub>2</sub> upon heating for the Mg–Al LDH samples (Mg/Al  $\approx$  2): (a) LDH[1h], (b) LDH[4h], (c) LDH[16h], and (d) LDH[72h].

evolution ( $\text{CO}_2$  and  $\text{H}_2\text{O}$ ) behaviors were measured under heating at a constant rate of  $10\text{ K min}^{-1}$ , as shown in Figure 5. In addition, thermogravimetry differential thermal analysis (TG-DTA) was performed for the various samples, and the results are presented in Figure S2. As indicated by Figure 5, all the samples exhibited three-step gas evolution behavior, which was particularly clear for the LDH[72h] specimen (Figure 5d). In our recent study,<sup>26,27</sup> we obtained atomic/molecular-level pictures of these multistep chemical and structural transformations of Mg–Al LDHs at elevated temperatures. These transformations consist of three steps: (1) the release of interlayer water, (2) partial dehydroxylation of the hydroxyl layers followed by coordination of carbonate ions to the metals, and (3) collapse of the layered structure.<sup>26,27</sup> As shown in Figure 5, all the samples tested exhibited the distinct three-step transformation behavior corresponding to steps (1)–(3), regardless of the particle size.

Importantly, differences in the gas evolution behaviors of the various samples were observed in the CO<sub>2</sub> evolution amounts in step (2). Specifically, between 530 and 650 K, considerable amounts of CO<sub>2</sub> were released, which increased in the following order: LDH[72h] < LDH[16h] < LDH[4h] < LDH[1h]. These results indicated that within this temperature range, a larger amount of CO<sub>2</sub> was released as the particle size was reduced, likely owing to the larger BET surface areas of the samples (Table 2). However, the origin of CO<sub>2</sub> release over this temperature range remains unclear. In our previous study,<sup>27</sup> two possible origins of CO<sub>2</sub> release were proposed: the adsorbed CO<sub>2</sub> present on the outer surfaces of the LDH particles and interlayer CO<sub>3</sub><sup>2-</sup> anions.<sup>27</sup> This will be discussed in detail later in the paper.

From the viewpoint of applying these materials as CO<sub>2</sub> adsorbents, it is essential to acknowledge that considerable amounts of CO<sub>2</sub> were released at temperatures of <603 K, and the

Table 2. CO<sub>2</sub> evolution amounts recorded for steps (1)–(3) of the chemical/structural transformations.

Sample	CO <sub>2</sub> evolution amount / 10 <sup>-3</sup> mol g <sup>-1</sup>			total
	step (1) (437–539 K)	step (2) (539–669 K)	step (3) (>669 K)	
LDH[1h]	0.05	0.42	0.91	1.38
LDH[4h]	0.02	0.24	0.87	1.14
LDH[16h]	0.03	0.16	0.81	1.00
LDH[72h]	trace	0.08	1.10	1.18

layered structure was maintained during steps (1) and (2).<sup>26,27</sup> This suggests that these materials may be suitable for use as CO<sub>2</sub> adsorbents in TSA within the temperature ranges of steps (1) and (2): according to the CO<sub>2</sub> release behavior shown in Figure 5, TSA cycle between 463 and 603 K is expected to work, hopefully without the collapse of the layered structure of the LDH materials.

As mentioned previously, one advantage of these CO<sub>2</sub> gas evolution measurements is that they are quantitative. Table 2 presents the CO<sub>2</sub> evolution amounts recorded for the three transformation steps of the four LDH samples; the adsorption/desorption mechanism is discussed in a later section on the basis of these quantitative results.

The Mg/Al ratios were close to 2 and significantly smaller than 3 for the samples evaluated in this study. As reported in our previous study,<sup>27</sup> large differences were observed in the multistep gas evolution behaviors of Mg–Al LDH samples with different Mg/Al ratios, wherein the three distinct steps were only observed for LDHs with Mg/Al = 2. This characteristic is advantageous because it allows these materials to be used as adsorbents at temperatures below the point of structural collapse.

### **CO<sub>2</sub> Capture Capacities in Repeated Temperature Swing Adsorption/Desorption Cycles**

Subsequently, the CO<sub>2</sub> gas evolution behaviors of the LDH samples were examined under TSA cycling. For this purpose, two sets of adsorption conditions (“wet” and “dry” conditions) were applied, as shown in Figure 6. Under wet conditions, 35.5 kPa of H<sub>2</sub>O vapor was added to the gas flow in the adsorption step, whereas no water vapor was added in the dry experiments. In the desorption steps of both the wet and dry experiments, the samples were heated from 463 to 603 K at a rate of 10 K min<sup>-1</sup> under a dry flow of Ar. Subsequently, the target temperature was maintained for 15 min.

The CO<sub>2</sub> desorption amounts for the repeated TSA cycle experiments are shown in Figure 6. The word “initial” in the abscissa indicates that the fresh sample was heated from 463 to 603 K without employing a CO<sub>2</sub> adsorption procedure, and the desorbed CO<sub>2</sub> was quantified during heating. That is, the “initial” CO<sub>2</sub> desorption is originated from carbonate species that were contained in the fresh adsorbents. Subsequently, the CO<sub>2</sub> adsorption procedure under “dry” and “wet” conditions was conducted, followed by heating from 463 to 603 K under an Ar flow, with the CO<sub>2</sub> desorption measured as “cycle 1”.

As shown in Figure 6a, under dry conditions, the CO<sub>2</sub> desorption amounts for cycle 1 were smaller than the corresponding “initial” results. With an increase in the cycle number, the CO<sub>2</sub> desorption amount for the LDH[1h] specimen gradually decreased from ~0.16 to 0.12 mol kg<sup>-1</sup>, while those of the LDH[4h], LDH[16h], and LDH[72h] samples exhibited less pronounced

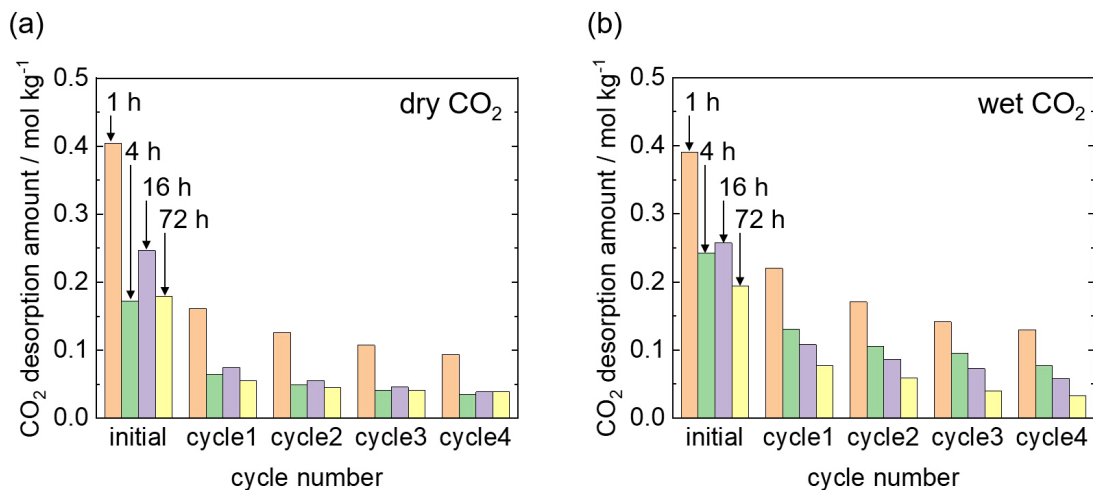


**Figure 6.** CO<sub>2</sub> desorption amounts over repeated TSA cycles for the Mg–Al LDH samples under (a) dry conditions and (b) wet conditions.



reductions (Figure 6a). In other words, under dry condition, the LDH[4h], LDH[16h], and LDH[72h] samples exhibited low CO<sub>2</sub> desorption amounts from the cycle 1. A comparison of Figures 6a and 6b indicates the effect of the H<sub>2</sub>O vapor. Specifically, under wet conditions (Figure 6b), the CO<sub>2</sub> desorption was enhanced for all the samples. The durability was also enhanced for LDH[1h], LDH[4h], and LDH[16h] samples. Furthermore, the four samples exhibited different CO<sub>2</sub> desorption amounts depending on the particle size and/or surface area, which decreased in the following order: LDH[1h] > LDH[4h] > LDH[16h] > LDH[72h]. The positive effect of H<sub>2</sub>O vapor on the performance of the CO<sub>2</sub> adsorbents can be explained with reference to the molecular-level adsorption/desorption mechanism of CO<sub>2</sub>. One possible reason is related to the “memory effect”: H<sub>2</sub>O vapor could enhance the stability of the layered structure of LDHs. Another possible reason is that interlayer carbonate species could be involved in the desorption reaction. These points will be discussed in a later section.

To obtain further information regarding the potential of these LDH materials to adsorb CO<sub>2</sub> from the air via direct air capture (DAC), repeated TSA experiments were conducted at a low CO<sub>2</sub> concentration of 400 ppm using the LDH [4h] sample, as shown in Figure 7. Note that the word “initial” in the abscissa is used with the same meaning as in Fig. 6. The CO<sub>2</sub> desorption amounts were significantly reduced compared with those observed in Figure 6, indicating that under the operating conditions adopted, these materials are not promising for application as DAC adsorbents.

### **Quantitative Discussion of Origin of CO<sub>2</sub> Evolution/Desorption in Step (2) (463–603 K)**

Following confirmation that the Mg–Al LDH ( $\text{Mg}/\text{Al} \approx 2$ ) nanoparticle/microparticle samples released  $\text{CO}_2$  at temperatures of  $\sim 600$  K while maintaining their layered structures (Figure 5 and Table 2), the amount of  $\text{CO}_2$  evolution/desorption was assessed with respect to the BET surface areas and the particle sizes. If the released  $\text{CO}_2$  originates from the particle surfaces, the amount of  $\text{CO}_2$  evolved should be proportional to the BET surface area of the sample. However, if the  $\text{CO}_2$  originates from the interlayer  $\text{CO}_3^{2-}$  species, the amount of evolved  $\text{CO}_2$  should be proportional to the total side surface areas of the plate-like particles. Analysis of the contributions of different crystal planes is essential for obtaining deep insights into the surface functions of crystalline materials, as reported for solid catalysts<sup>41,42</sup> and photocatalysts.<sup>43,44</sup> Thus, we calculated the total side surfaces  $S_{\text{side}}$  according to the SEM-derived particle sizes and the

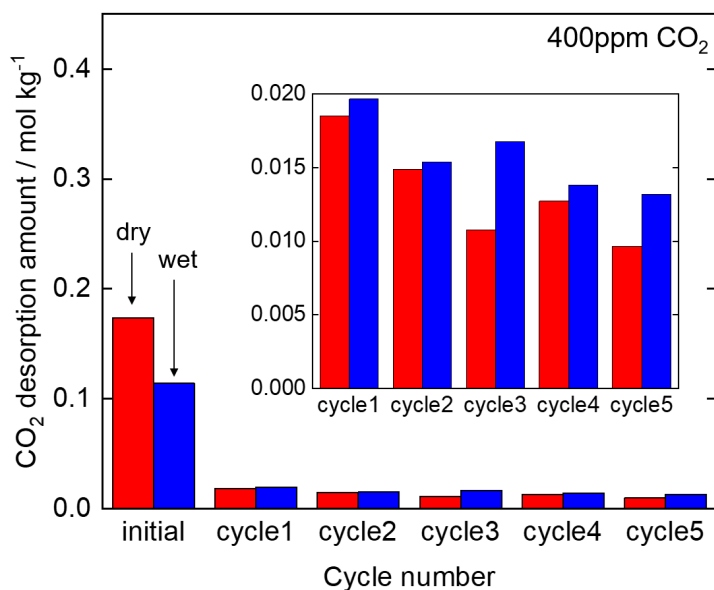


**Figure 7.**  $\text{CO}_2$  desorption amounts in the repeated TSA cycles using dilute  $\text{CO}_2$  gas (400 ppm  $\text{CO}_2$  in Ar) under dry and wet conditions. LDH[4h] was used as the sample. See the text for details.

calculated crystal density. From the SEM images, we counted the plate-like particles and measured their diameters by using an image processing software ImageJ.  $S_{\text{side}}$  values were calculated for the four samples using the data and density of the LDH crystal, assuming that the particles have the same thickness in each sample. According to the results presented in Table 1, the  $S_{\text{side}}/S_{\text{BET}}$  ratios were similar for all the samples (i.e., 0.14–0.16), indicating that their aspect ratios and particle shapes were similar. As shown in Figure S3, the amounts of released  $\text{CO}_2$  were linearly correlated with both  $S_{\text{BET}}$  and  $S_{\text{side}}$ . Thus, these results fail to confirm the origin of the released  $\text{CO}_2$ . To address this issue, it is necessary to prepare LDH samples with different aspect ratios and compare their  $\text{CO}_2$  evolution behaviors.

### **Structural Analyses of Adsorbed Species and Adsorbents Using *In Situ* FT-IR Spectroscopy and *In Situ* XRD**

*In situ* FT-IR measurement was performed to examine the  $\text{CO}_2$  adsorption mechanism over repeated TSA cycles in the presence and absence of  $\text{H}_2\text{O}$  vapor. In these measurements, it was impossible to use the same conditions that were employed in the TSA experiments, because of limitations related to the  $\text{H}_2\text{O}$  pressure. Thus, the experimental conditions and procedures were selected to reproduce the phenomena occurring over repeated TSA cycles to the greatest extent possible. LDH[4h] was used as a representative sample for these measurements.

The FT-IR experiments were initially performed without H<sub>2</sub>O vapor to imitate dry conditions. The IR signals of the adsorbed species were extracted from the raw spectra shown in Figure 8a, and the corresponding subtracted spectra are presented in Figure 8b. Initially, the fresh samples were evacuated at both room temperature and 463 K, and as shown in Figure 8a, an intense absorption peak appeared at 1350 cm<sup>-1</sup>. This peak was assigned to the interlayer CO<sub>3</sub><sup>2-</sup> species that were hydrogen-bonded to interlayer water molecules.<sup>26,27</sup> After the evacuation at 463 K, the peak at 1350 cm<sup>-1</sup> remained, and a new peak appeared at 1530 cm<sup>-1</sup>, corresponding to the CO<sub>3</sub><sup>2-</sup> species that lost their hydrogen bonds with water.<sup>26,27</sup> These results suggest that only some interlayer water molecules were removed at this temperature, rendering step (1) incomplete, which is consistent with our previous study.<sup>26,27</sup> Following the evacuation of the sample at 603 K,

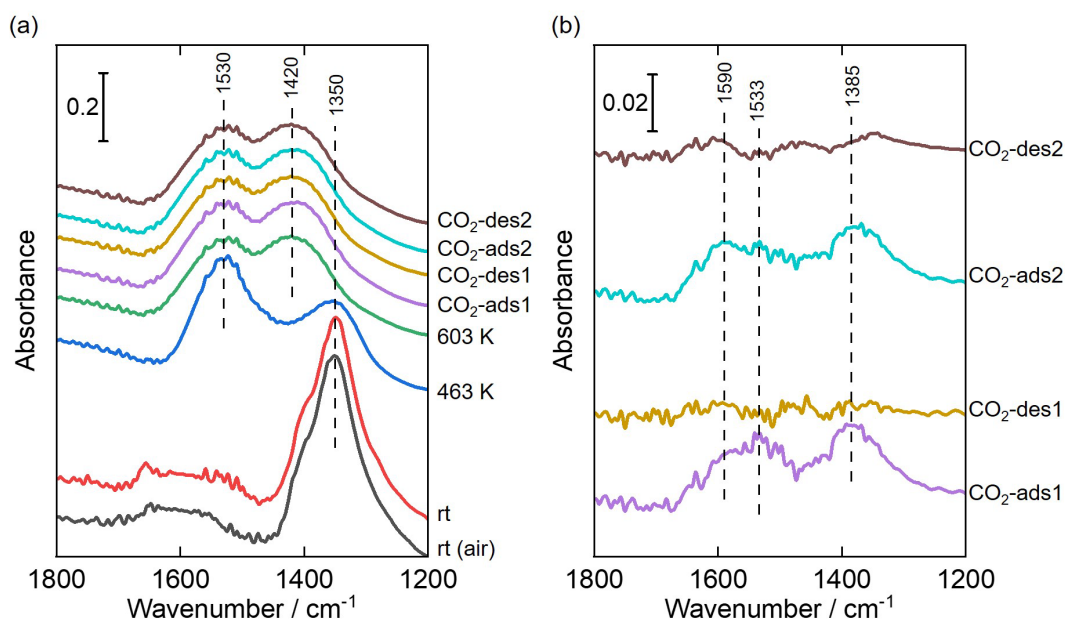


**Figure 8.** *In situ* FT-IR spectra recorded during repeated CO<sub>2</sub> adsorption/desorption cycles under dry conditions: (a) raw spectra and (b) subtracted spectra. LDH[4h] was used as a representative sample.

split peaks were observed at 1420 and 1530  $\text{cm}^{-1}$ . The split width of 110  $\text{cm}^{-1}$  is smaller than 300  $\text{cm}^{-1}$ , indicating that a monodentate carbonate species was present.<sup>40</sup> This interpretation is consistent with the IR band positions simulated by the first-principles DFT calculations, as presented in Table S1 (SI). As indicated by previous studies,<sup>26,27</sup> the heating of Mg–Al LDH (Mg/Al  $\approx$  2) at 603 K induces a structural transformation in which the hydroxide layer is partially dehydroxylated. According to our previous studies,<sup>26,27</sup> one third or more of the hydroxyl groups are eliminated from the LDH crystals (Mg/Al  $\approx$  2) to form coordinatively unsaturated sites and release water molecules.<sup>26,27</sup> Simultaneously, interlayer  $\text{CO}_3^{2-}$  anions react with almost half of the unsaturated sites to form monodentate carbonate species in the interlayer spaces. This structural transformation was referred to as step (2).<sup>26,27</sup> The reaction scheme in step (2) is involved in Scheme 1. Thus, the 603 K spectrum presented in Figure 8a corresponds to monodentate  $\text{CO}_3^{2-}$  ions coordinating with two  $\text{Mg}^{2+}$  ions and one  $\text{Al}^{3+}$  ion.<sup>26,27,45</sup>

Subsequently, the LDH[4h] sample was exposed to 80 kPa of gaseous  $\text{CO}_2$  at 463 K after cooling from 603 K in vacuum conditions. To detect the spectrum of the adsorbed species, the spectrum before adsorption (spectrum 603 K in Figure 8a) was subtracted from that after adsorption, yielding the  $\text{CO}_2$ -ads1 spectrum shown in Figure 8b. The spectrum contained two IR absorption peaks at 1385 and 1533  $\text{cm}^{-1}$ , which differed from the two split peaks assigned to the monodentate  $\text{CO}_3^{2-}$  species (i.e., at 1420 and 1530  $\text{cm}^{-1}$ ). These peaks appeared close to those recorded for the sample evacuated at 463 K; for that sample, the peaks at 1350 and 1530  $\text{cm}^{-1}$  were attributed to the interlayer  $\text{CO}_3^{2-}$  species with and without hydrogen bonding, respectively. This is discussed later with reference to the *in situ* XRD results. After subsequent evacuation of this sample at 603 K, a flat spectrum was obtained through subtraction ( $\text{CO}_2$ -des1, Figure 8b), indicating that the adsorption/desorption process was reversible. This procedure (exposure to

CO<sub>2</sub> at 463 K and evacuation at 603 K) was then repeated. The resulting spectrum (CO<sub>2</sub>-ads2) was similar to that obtained following the first cycle (CO<sub>2</sub>-ads1). After the second evacuation at 603 K (CO<sub>2</sub>-des2), it was clear that the adsorbed species had been released again.

*In situ* powder XRD experiments were performed to trace the layered crystal structure of the sample during the CO<sub>2</sub> adsorption/desorption process (Figure 9). Initially, the dry measurement conditions were adopted (Figure 9a), and the sample evacuated at 463 K exhibited an intense sharp peak (indexed as 003) with an interlayer distance of 7.37 Å. Notably, this interlayer distance was slightly smaller than that of the sample under ambient conditions (7.62 Å, indicated as “rt” in Figure 9a). In addition, the diffraction caused by the periodicity with a half interlayer distance of  $2\theta \approx 24^\circ$  (indexed as 006) was still observed clearly. According to our previous study,

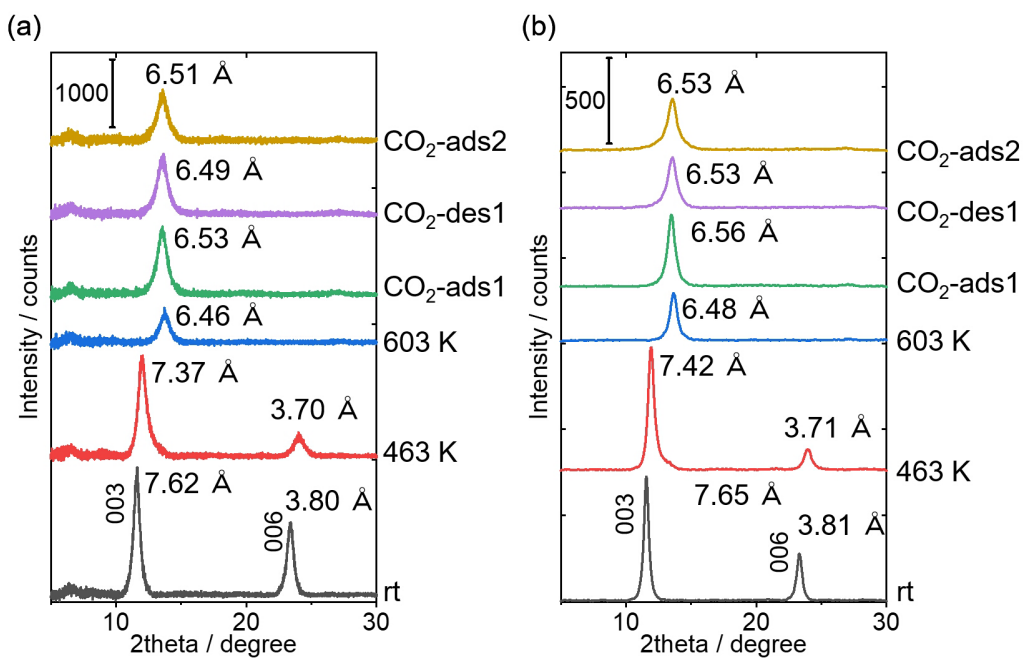


**Figure 9.** *In situ* XRD patterns recorded during repeated CO<sub>2</sub> adsorption/desorption experiments under (a) dry conditions and (b) wet conditions. LDH[4h] was used as a representative sample.

when the interlayer water molecules are eliminated, the interlayer distance decreases significantly (by  $\sim 0.9$  Å) owing to the waving of the metal hydroxide layers, as indicated by the crystal structural model optimized in our previous study.<sup>27</sup> Additionally, the 006 diffraction is considerably weakened.<sup>27</sup> Thus, the present results are consistent with the interpretation that many water molecules remain in the interlayer spaces. According to our previous study<sup>27</sup>, when the sample is evacuated at 603 K, the interlayer water molecules are eliminated, and the transformation (step (2)) occurs. The observed interlayer distance was 6.46 Å, and the 006 diffraction almost disappeared accordingly (603 K, Figure 9a). Upon subsequent exposure of the sample to gaseous CO<sub>2</sub> at 463 K, the interlayer distance increased slightly, from 6.46 to 6.53 Å (CO<sub>2</sub>-ads1, Figure 9a). Considering this result along with that presented above for the FT-IR experiments (Figure 8b), it is likely that upon exposure to gaseous CO<sub>2</sub> at 603 K under dry conditions, a certain amount of CO<sub>2</sub> was inserted as interlayer CO<sub>3</sub><sup>2-</sup> species both with and without hydrogen bonding to water molecules.

Successive *in situ* FT-IR and XRD experiments were conducted during the second adsorption/desorption cycle, and overall, the results were similar to those obtained in the first cycle. However, after the second cycle, a new peak appeared at  $\sim 1590$  cm<sup>-1</sup> (CO<sub>2</sub>-ads2, Figure 8b), in addition to the two peaks observed for the first CO<sub>2</sub> adsorption (1533 and 1385 cm<sup>-1</sup>, CO<sub>2</sub>-ads1, Figure 8b). It was considered that this new peak reflected slight differences in the states and structures of the adsorbed species. In the *in situ* XRD results presented in Figure 9a, small and almost reversible changes in the interlayer distance were observed during the repeated CO<sub>2</sub> adsorption/desorption cycles: at 603 K, the distance varied from 6.46 to 6.53, 6.49, and 6.51 Å for CO<sub>2</sub>-ads1, CO<sub>2</sub>-des1 and CO<sub>2</sub>-ads2, respectively, as shown in Figure 9a. These variations suggest that gaseous CO<sub>2</sub> molecules were partly inserted into the interlayer spaces to form

interlayer  $\text{CO}_3^{2-}$  ions that could be reversibly removed. Mg–Al LDH ( $\text{Mg}/\text{Al} \approx 2$ ) was partially dehydroxylated when it was heated to 603 K (after step (2)), and oxide anions were present on the layers (oxygen highlighted in red in the models **1** and **2** in Scheme 1). Furthermore, in the “initial” steps in the TSA cycling (Figure 6), considerable amounts of  $\text{CO}_2$  were released. These  $\text{CO}_2$  evolutions are due to decomposition of  $\text{CO}_3^{2-}$  species (the final step in Scheme 1): one  $\text{O}^{2-}$  ion is left on the surface after the decomposition of one carbonate ion (red oxygen in the models **3** and **4** in Scheme 2). Such oxide ions can react with  $\text{CO}_2$  molecules to form interlayer  $\text{CO}_3^{2-}$  ions. The structural optimization results presented in Scheme S1 (SI) suggest that stability of the adsorbed species significantly depends on the local structure of the adsorption site. This point is an interesting subject for future studies.

Subsequently, *in situ* FT-IR (Figure 10) and XRD (Figure 9b) experiments were performed under the simulated wet conditions. Exposure to  $\text{H}_2\text{O}$  vapor at room temperature produced two IR absorption peaks at 1512 and 1376  $\text{cm}^{-1}$  ( $\text{H}_2\text{O}$ -ads, Figure 10b). This was unexpected, because no  $\text{CO}_2$  was introduced into the system during this step. A possible explanation is that carbonate species and/or adsorbed  $\text{CO}_2$  molecules, whose IR absorption signals are relatively weak, were present on the outer surfaces of the particles and/or interlayer spaces and that they interacted with the  $\text{H}_2\text{O}$  molecules at room temperature to produce strong signals. With subsequent exposure to gaseous  $\text{CO}_2$  at 463 K, the IR band at a larger wavenumber became broader in the subtracted spectrum ( $\text{CO}_2$ -ads, Figure 10b). Specifically, a new IR peak appeared at 1580  $\text{cm}^{-1}$ , which was at a similar position to that observed following the second adsorption under dry conditions (1590  $\text{cm}^{-1}$ ,  $\text{CO}_2$ -ads2, Figure 8b). Currently, it is impossible to provide an exact assignment for this signal. Subsequently, significant spectral changes were observed after evacuation at 603 K ( $\text{CO}_2$ -des, Figure 10b). For example, the absorption bands observed in the



CO<sub>2</sub>-ads spectrum disappeared, and two inverse peaks appeared at 1527 and 1405 cm<sup>-1</sup>; notably, the emergence of inverse IR peaks was not observed in the dry experiments (Figure 8). Thus, the results presented in Figure 10b suggest that the adsorbed species formed when the sample was exposed to CO<sub>2</sub> were completely and reversibly removed during evacuation at 603 K. Furthermore, under wet conditions (i.e., with pre-adsorbed water vapor), the carbonate species producing signals at 1527 and 1405 cm<sup>-1</sup> were removed. Peaks similar to those recorded for the LDH samples heated to 603 K (Figure 8a) were observed. In our previous study, these peaks were assigned to the monodentate CO<sub>3</sub><sup>2-</sup> species coordinated with two Mg<sup>2+</sup> and one Al<sup>3+</sup> ions.

The *in situ* XRD results obtained under the wet conditions are presented in Figure 9b. As shown, during the initial CO<sub>2</sub> adsorption process (CO<sub>2</sub>-ads1), the interlayer distance increased

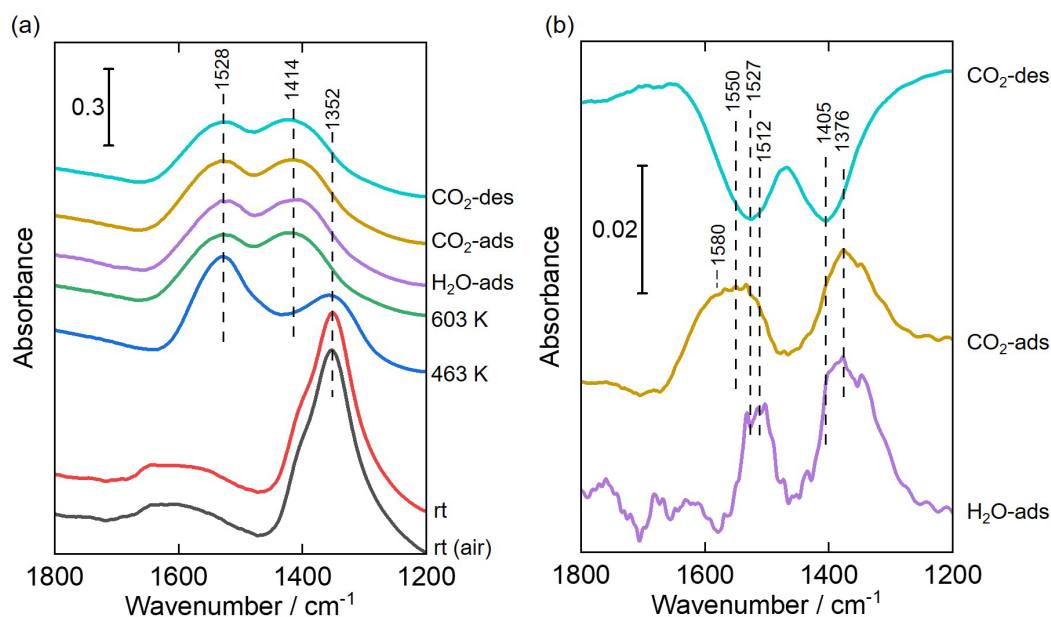


**Figure 10.** *In situ* FT-IR spectra recorded during CO<sub>2</sub> adsorption/desorption cycling under wet conditions: (a) raw spectra and (b) subtracted spectra. LDH[4h] was used as a representative sample.

from 6.48 to 6.56 Å. Subsequently, during the first desorption process (CO<sub>2</sub>-des1), the interlayer distance decreased from 6.56 to 6.53 Å. Considering the *in situ* FT-IR results, this reduction under wet conditions was likely due to the desorption of interlayer species (e.g., monodentate CO<sub>3</sub><sup>2-</sup>), which explains the inverse peaks shown in the CO<sub>2</sub>-des spectrum of Figure 8b. Thus, the XRD results confirm the insertion and desorption of carbonate species within the interlayer species. However, it is unclear why the interlayer distance did not change in the subsequent CO<sub>2</sub> adsorption cycle (CO<sub>2</sub>-ads2, Figure 9b).

According to the *in situ* XRD results presented in Figures 9a and b, the adsorbent maintained its layered crystal structure after repeated CO<sub>2</sub> adsorption/desorption cycles. This can be explained by the fact that the desorption temperature (603 K) was within the range required to complete steps (1) and (2) and was lower than the temperature at which step (3) (collapse of the layered structure) begins. Next, we investigated whether the layered structure was maintained after repeated TSA cycles, such as those presented in Figure 6. As shown in Figure S4, the layered structure finally disappeared upon repeated cycling, and a broad diffraction assignable to the cubic rock-salt structure was observed. These results indicate that repeated TSA cycles led to structural collapse. However, Mg–Al LDH crystals are known to exhibit a “memory effect” after degradation at high temperatures. In the “memory effect”, following the production of mixed oxides with amorphous or poorly crystallized rock-salt structures, the layered structure is known to be recovered in the presence of H<sub>2</sub>O. Therefore, this memory effect may have the potential to enhance the structural durability and increase the adsorption capacity over repeated TSA cycles—particularly under wet conditions.

## Mechanistic Aspects of Adsorption and Desorption Phenomena during Repeated TSA Cycles

As described above, during the TSA adsorption/desorption cycles, CO<sub>2</sub> evolved in the temperature range of 463–603 K. When the Mg–Al LDH sample was heated to 603 K, a structural transformation occurred (step (2)), wherein the hydroxide layers were partially dehydroxylated to form coordinatively unsaturated sites, followed by coordination of carbonate ions to the metal ions (Scheme I). The *in situ* FT-IR results indicated that the adsorption/desorption phenomena differed significantly under dry and wet conditions. Specifically, the results obtained under wet conditions indicated that the interlayer monodentate carbonate species could be involved in the desorption reaction. This suggests a potential material advantage, because if the sites in the interlayer spaces are available for both the adsorption and desorption of CO<sub>2</sub>, the capacity of the adsorbent is expected to be increased significantly. However, the repeated removal of interlayer carbonate species is expected to accelerate the degradation of the layered crystal structure, because the interlayer anions are vital pillars between the layers in the LDH crystal structure. The experiments described herein suggested that this layered structure was degraded, implying that the stable intercalation of suitably bulky anions into the interlayer spaces can enhance the durability of the layered structure, along with the adsorbent capacity. This should be examined in future studies. The structural optimization results presented in Scheme S1 (SI) suggest that stability of the adsorbed species significantly depends on the local structure of the adsorption site. This point is also an interesting subject for future studies.

## CONCLUSIONS

Mg–Al layered double hydroxide (LDH, Mg/Al  $\approx$  2) nanoparticles/microparticles were prepared via a hydrothermal synthetic route, and their potential performance as CO<sub>2</sub> adsorbents for TSA was investigated. The particle size was systematically controlled by varying the hydrothermal treatment duration. The properties of the samples were characterized using various analytical techniques to obtain information regarding the chemical compositions, water contents, particle diameters, outer surface areas, crystal thicknesses, and total surface areas of the side faces of the plate-like particles. The gas evolution behaviors of samples with different particle sizes were measured quantitatively during continuous heating. A distinct three-step gas evolution process was observed for all the samples, corresponding to multistep structural and chemical transformations. During step (2), which was proved in our previous studies<sup>26,27</sup> to correspond to partial dehydroxylation of the hydroxyl layers followed by the coordination of carbonate ions to the metal ions, significant amounts of CO<sub>2</sub> evolved at temperatures lower than the temperature needed to initiate the collapse of the layered crystal structure. Furthermore, the CO<sub>2</sub> evolution amount increased as the particle size decreased. It was considered that the evolved CO<sub>2</sub> originated from either species adsorbed on the outer surfaces of the LDH particles or interlayer CO<sub>3</sub><sup>2-</sup> anions in the peripheral parts of the plate-like particles. These two possibilities were evaluated by comparing the correlations of the CO<sub>2</sub> evolution amounts with the BET surface areas and the total areas of the side faces. However, the observed trends were similar; thus, no clear conclusion could be drawn. Subsequently, the CO<sub>2</sub> desorption amounts were measured over repeated TSA cycles between 463 and 603 K. The investigated samples exhibited high CO<sub>2</sub> desorption capacities, and the presence of water vapor enhanced their performance. Moreover, combining the experimental results with the findings of *in situ* FT-IR and XRD revealed that the adsorption/desorption cycles were reversible, and the interlayer distance increased and decreased

after the adsorption and desorption procedures, respectively. These results suggest that a certain amount of carbonate species was inserted into the interlayer spaces of the LDHs during adsorption and that these species were removed during desorption.

Overall, the present study indicates the potential performance of Mg–Al LDH ( $\text{Mg/Al} \approx 2$ ) nanoparticles/microparticles as  $\text{CO}_2$  adsorbents over the temperature range of 463–603 K. Intercalation of suitably bulky anions into the interlayer spaces can enhance the durability of the layered structure, along with the adsorbent capacity. Future research should focus on the use of supports such as alumina to develop materials suitable for use in practical applications.

## ASSOCIATED CONTENT

### Supporting Information

The Supporting Information is available free of charge at .....

Optimized structural models for adsorbed species and calculated infrared absorption positions by first-principles DFT calculations, lattice parameters and chemical compositions of the samples,  $\text{N}_2$  adsorption isotherms, TG-DTA results, correlations of  $\text{CO}_2$  evolution/desorption amounts with BET surface areas or areas of side faces of the plate-like particles, XRD patterns of the samples after TSA cycles (PDF).

## AUTHOR INFORMATION

### Corresponding Author

Kei Inumaru – Graduate School of Advanced Science and Engineering, Hiroshima University, 1-4-1, Kagamiyama, Higashihiroshima, Hiroshima 739-8527, Japan; [orcid.org/0000-0001-6876-3854](https://orcid.org/0000-0001-6876-3854); E-mail: [inumaru@hiroshima-u.ac.jp](mailto:inumaru@hiroshima-u.ac.jp)

## **Authors**

Mio Kawashimo – Graduate School of Advanced Science and Engineering, Hiroshima University, 1-4-1, Kagamiyama, Higashihiroshima, Hiroshima 739-8527, Japan

Kaito Matsuda – Graduate School of Advanced Science and Engineering, Hiroshima University, 1-4-1, Kagamiyama, Higashihiroshima, Hiroshima 739-8527, Japan

Ryuta Okumiya – Graduate School of Advanced Science and Engineering, Hiroshima University, 1-4-1, Kagamiyama, Higashihiroshima, Hiroshima 739-8527, Japan

Nana Iio – Graduate School of Advanced Science and Engineering, Hiroshima University, 1-4-1, Kagamiyama, Higashihiroshima, Hiroshima 739-8527, Japan

Ayaka Okuda – Graduate School of Advanced Science and Engineering, Hiroshima University, 1-4-1, Kagamiyama, Higashihiroshima, Hiroshima 739-8527, Japan

Ryota Fukuzaki – Graduate School of Advanced Science and Engineering, Hiroshima University, 1-4-1, Kagamiyama, Higashihiroshima, Hiroshima 739-8527, Japan

Naoki Tarutani – Graduate School of Advanced Science and Engineering, Hiroshima University, 1-4-1, Kagamiyama, Higashihiroshima, Hiroshima 739-8527, Japan; [orcid.org/0000-0003-0696-8082](https://orcid.org/0000-0003-0696-8082)

Kiyofumi Katagiri – Graduate School of Advanced Science and Engineering, Hiroshima University, 1-4-1, Kagamiyama, Higashihiroshima, Hiroshima 739-8527, Japan; orcid.org/0000-0002-9548-9835

## Notes

The authors declare no competing financial interests.

## ACKNOWLEDGMENT

This work was partly supported by JSPS KAKENHI (Grant Numbers JP18H01709, JP23H00236, JP22H05143, and JP23KJ1624), JST ACT–C (Grant Number JPMJCR12Y2), JST the establishment of university fellowships towards the creation of science technology innovation (Grant Number JPMJFS2129), and the JST-Mirai Program (Grant Number JPMJMI22E3).

## REFERENCES

- (1) *Layered Double Hydroxides (Structure and Bonding, 119)*; Duan, X., Evans, D. G., Eds.; Springer: Berlin, 2006.
- (2) Ebitani, K.; Motokura, K.; Mori, K.; Mizugaki, T.; Kaneda, K. Reconstructed Hydrotalcite as a Highly Active Heterogeneous Base Catalyst for Carbon-Carbon Bond Formations in the Presence of Water. *J. Org. Chem.*, **2006**, *71*, 5440–5447. DOI: 10.1021/jo060345l

- (3) Cantrell, D. G.; Gillie, L. J.; Lee, F.; Wilson, K. Structure-Reactivity Correlations in MgAl Hydrotalcite Catalysts for Biodiesel Synthesis. *Appl. Catal. A:General*, **2005**, *287*, 183–190. DOI: 10.1016/j.apcata.2005.03.027
- (4) Nishimura, S.; Takagaki, A.; Ebitani, K. Characterization, Synthesis and Catalysis of Hydrotalcite-Related Materials for Highly Efficient Materials Transformations. *Green Chem.*, **2013**, *15*, 2026–2042. DOI: 10.1039/c3gc40405f
- (5) Teramura, K.; Iguchi, S.; Mizuno, Y.; Shishido, T.; Tanaka, T. Photocatalytic Conversion of CO<sub>2</sub> in Water over Layered Double Hydroxides. *Angew. Chem. Int. Ed.*, **2012**, *51*, 8008–8011. DOI: 10.1002/anie.201201847
- (6) Iguchi, S.; Teramura, K.; Hosokawa, S.; Tanaka, T. Photocatalytic Conversion of CO<sub>2</sub> in an Aqueous Solution using Various Kinds of Layered Double Hydroxides. *Catal. Today*, **2015**, *251*, 140–144. DOI: 10.1016/j.cattod.2014.09.005
- (7) Sudare, T.; Yamaguchi, T.; Ueda, M.; Shiiba, H.; Tanaka, H.; Tipplook, M.; Hayashi, F.; Teshima, K. Critical Role of Water Structure around Interlayer Ions for Ion Storage in Layered Double Hydroxides. *Nat. Commun.*, **2022**, *13*, Art. No. 6448. DOI: 10.1038/s41467-022-34124-9
- (8) Ma, H.-N.; He, J.; Xiong, D.-B.; Wu, J.-S.; Li, Q.-Q.; Dravid, V.; Zhao, Y.-F. Nickel Cobalt Hydroxide @Reduced Graphene Oxide Hybrid Nanolayers for High Performance Asymmetric Supercapacitors with Remarkable Cycling Stability. *ACS Appl. Mater. Interfaces*, **2016**, *8*, 1992–2000. DOI: 10.1021/acsami.5b10280
- (9) Burke, M. S.; Kast, M. G.; Trotochaud, L.; Smith, A. M.; Boettcher, S. W. Cobalt-Iron (Oxy)Hydroxide Oxygen Evolution Electrocatalysts: The Role of Structure and Composition



- on Activity, Stability, and Mechanism. *J. Am. Chem. Soc.*, **2015**, *137*, 3638–3648. DOI: 10.1021/jacs.5b00281
- (10) Louie, M. W.; Bell, A. T. An Investigation of Thin-film Ni-Fe Oxide Catalysts for the Electrochemical Evolution of Oxygen. *J. Am. Chem. Soc.*, **2013**, *135*, 12329–12337. DOI: 10.1021/ja405351s
- (11) Li, C.; Wei, M.; Evans, D. G.; Duan, X. Layered Double Hydroxide-based Nanomaterials as Highly Efficient Catalysts and Adsorbent. *Small*, **2014**, *10*, 4469–4486. DOI: 10.1002/sml.201401464
- (12) Wang, Q.; Gao, Y. Luo, J.; Zhong, Z.; Borgna, A.; Guo, Z.; O'Hare, D. Synthesis of Nano-Sized Spherical  $\text{Mg}_3\text{Al-CO}_3$  Layered Double Hydroxide as a High-Temperature  $\text{CO}_2$  Adsorbent. *RSC Adv.*, **2013**, *3*, 3414–3420. DOI: 10.1039/c2ra22607c
- (13) Kameda, T.; Nagano, S.; Kumagai, S. Saito, Y.; Yoshioka, T. Enrichment of Carbon Dioxide using Mg–Al Layered Double Hydroxides, *Chem. Eng. Res. Des.*, **2023**, *194*, 318–324. DOI: 10.1016/j.cherd.2023.04.065
- (14) Yang, W.; Kim, Y.; Liu, P. K. T.; Sahimi, M.; Tsotsis, T. T. A Study by *In situ* Techniques of the Thermal Evolution of the Structure of a Mg-Al- $\text{CO}_3$  Layered Double Hydroxide. *Chem. Eng. Sci.*, **2002**, *57*, 2945–2953. DOI: 10.1016/S0009-2509(02)00185-9
- (15) Bellotto, M.; Rebours, B.; Clause, O.; Lynch, J.; Bazin, D.; Elkaïm, E. A Reexamination of Hydrotalcite Crystal Chemistry. *J. Phys. Chem.*, **1996**, *100*, 8527–8534. DOI: 10.1021/jp960039j
- (16) Bellotto, M.; Rebours, B.; Clause, O.; Lynch, J.; Bazin, D.; Elkaïm, E. Hydrotalcite Decomposition Mechanism: A Clue to the Structure and Reactivity of Spinel-Like Mixed Oxides. *J. Phys. Chem.*, **1996**, *100*, 8535–8542. DOI: 10.1021/jp960039j

- (17) Sasai, R.; Sato, H.; Sugata, M.; Fujimura, T.; Ishihara, S.; Deguchi, K.; Ohki, S.; Tansho, M.; Shimizu, T.; Oita, N. et al. Why Do Carbonate Anions Have Extremely High Stability in the Interlayer Space of Layered Double Hydroxides? Case Study of Layered Double Hydroxide Consisting of Mg and Al (Mg/Al = 2). *Inorg. Chem.*, **2019**, 58, 10928–10935. DOI: 10.1021/acs.inorgchem.9b01365
- (18) Yu, J.; Ruengkajorn, K.; Crivoi, D.-G.; Chen, C.; Buffet, J.-C.; O'Hare, D. High Gas Barrier Coating using Non-Toxic Nanosheet Dispersions for Flexible Food Packaging Film. *Nat. Commun.*, **2019**, 10, 2398. DOI: 10.1038/s41467-019-10362-2
- (19) León, M.; Díaz, E.; Bennici, S.; Vega, A.; Ordóñez, S.; Auroux, A. Adsorption of CO<sub>2</sub> on Hydrotalcite-Derived Mixed Oxides: Sorption Mechanisms and Consequences for Adsorption Irreversibility. *Ind. Eng. Chem. Res.*, **2010**, 49, 3663–3671. DOI: 10.1021/ie902072a
- (20) Zhang, J.; Xu, Y. F.; Qian, G.; Xu, Z. P.; Chen, C.; Liu, Q. Reinvestigation of Dehydration and Dehydroxylation of Hydrotalcite-Like Compounds through Combined TG-DTA-MS Analyses. *J. Phys. Chem. C*, **2010**, 114, 10768–10774. DOI: 10.1021/jp103115q
- (21) Kanazaki, E. Direct Observation of a Metastable Solid Phase of Mg/Al/CO<sub>3</sub>-Layered Double Hydroxide by Means of High Temperature *In Situ* Powder XRD and DTA/TG. *Inorg. Chem.*, **1998**, 37, 2588–2590. DOI: 10.1021/ic971543l
- (22) Rives, V. Comment on “Direct Observation of a Metastable Solid Phase of Mg/Al/CO<sub>3</sub>-Layered Double Hydroxide by Means of High Temperature *In Situ* Powder XRD and DTA/TG.”, *Inorg. Chem.*, **1999**, 38, 406–407. DOI: 10.1021/ic980739y

- (23) Gao, Y.; Zhang, Z.; Wu, J.; Yi, X.; Zheng, A.; Umar, A.; O'Hare D.; Wang, Q. Comprehensive Investigation of CO<sub>2</sub> Adsorption on Mg–Al–CO<sub>3</sub> LDH-Derived Mixed Metal Oxides *J. Mater. Chem. A*, **2013**, *1*, 12782–12790. DOI: 10.1039/c3ta13039h
- (24) Mascolo, G.; Mascolo, M. C. On the Synthesis of Layered Double Hydroxides (LDHs) by Reconstruction Method Based on the “Memory Effect”. *Microporous Mesoporous Mater.*, **2015**, *214*, 246–248, DOI: 10.1016/j.micromeso.2015.03.024
- (25) Millange, F.; Walton, R. I.; O'Hare, D. Time-Resolved *In Situ* X-ray Diffraction Study of the Liquid-Phase Reconstruction of Mg–Al–Carbonate Hydrotalcite-like Compounds, *J. Mater. Chem.*, **2000**, *10*, 1713–1720. DOI: 10.1039/b002827o
- (26) Matsuda, K.; Okuda, A.; Kawashimo, M.; Fukuzaki, R.; Iio, N.; Tarutani, N.; Katagiri, K.; Inumaru, K. Molecular-level Pictures of Chemical and Structural Transformations of Mg-Al Layered Double Hydroxide Crystals (Mg/Al = 2) at Elevated Temperatures. *J. Phys. Chem. C*, **2023**, *127*, 12599–12605. DOI: 10.1021/acs.jpcc.3c02859
- (27) Matsuda, K.; Iio, N.; Kawashimo, M.; Okuda, A.; Fukuzaki, R.; Tarutani, N.; Katagiri, K.; Inumaru, K. Comprehensive Analysis of the Chemical and Structural Transformations of Mg–Al–CO<sub>3</sub> Layered Double Hydroxides with Different Mg/Al Ratios at Elevated Temperatures. *Inorg. Chem.*, **2023**, *62*, 17276–17287. DOI: 10.1021/acs.inorgchem.3c02571
- (28) Tokudome, Y.; Morimoto, T.; Tarutani, N.; Vaz, P. D.; Nunes, C. D.; Prevot, V.; Stenning, G. B. G.; Takahashi, M. Layered Double Hydroxide Nanoclusters: Aqueous, Concentrated, Stable, and Catalytically Active Colloids toward Green Chemistry, *ACS Nano*, **2016**, *10*, 5550–5559. DOI: 10.1021/acsnano.6b02110
- (29) Tarutani, N.; Kimura, S.; Sakata, T.; Suzuki, K.; Katagiri, K.; Inumaru, K. Metal Hydroxide Salt Monolayer Nanoparticles: Synthesis, Redox Characterization, and

- Electrochemical Catalytic Performance. *ACS Materials Lett.*, **2022**, 4, 1430–1435. DOI: 10.1021/acsmaterialslett.2c00411
- (30) Kuroda, Y.; Miyamoto, Y.; Hibino, M.; Yamaguchi, K.; Mizuno, N. Tripodal Ligand-Stabilized Layered Double Hydroxide Nanoparticles with Highly Exchangeable  $\text{CO}_3^{2-}$ , *Chem. Mater.*, **2013**, 25, 2291–2296. DOI: 10.1021/cm400846k
- (31) Muramatsu, K.; Hayashi, S.; Kuroda, Y.; Oka, Y.; Wada, H.; Shimojima, A.; Kuroda, K. Selective Covalent Modification of Layered Double Hydroxide Nanoparticles with Tripodal Ligands on Outer and Interlayer Surfaces. *Inorg. Chem.*, **2020**, 59, 6110–6119. DOI: 10.1021/acs.inorgchem.0c00192
- (32) Wang, Q.; O'Hare, D. Recent Advances in the Synthesis and Application of Layered Double Hydroxide (LDH) Nanosheets. *Chem. Rev.*, **2012**, 112, 4124–4155. DOI: 10.1021/cr200434v
- (33) Vert, M.; Doi, Y.; Hellwich, K.; Hess, M.; Hodge, P.; Kubisa, P.; Rinaudo, M.; Schué, F. Terminology for Biorelated Polymers and Applications (IUPAC Recommendations 2012). *Pure Appl. Chem.*, **2012**, 84, 377–410. DOI: 10.1351/PAC-REC-10-12-04
- (34) Xu, Z.; Lu, G. Preparation of Suspensions. AU2005318862 B2, 2006.
- (35) Inumaru, K.; Katagiri, K.; Okuda, A.; Kawashimo, M. JP2020-138169A, 2020.
- (36) Inumaru, K.; Katagiri, K.; Iio, N. JP2019-42639A, 2019.
- (37) Baroni, S.; de Gironcoli, S.; dal Corso, A.; Giannozzi, P. Phonons and Related Crystal Properties from Density-Functional Perturbation Theory, *Rev. Mod. Phys.*, **2001**, 73, 515–562.

- (38) Gonze, X. First-principles Responses of Solids to Atomic Displacements and Homogeneous Electric Fields: Implementation of a Conjugate-Gradient Algorithm, *Phys. Rev. B*, **1997**, *55*, 10337–10354.
- (39) Misono, M. Heterogeneous Catalysis of Mixed Oxides Perovskite and Heteropoly Catalysts, *Stud. Surface Sci. Catal.*, **2013**, *176*, 1–181.
- (40) Nakamoto, K. *Infrared and Raman Spectra of Inorganic and Coordination Compounds*; John Wiley & Sons: Hoboken, 1997.
- (41) Inumaru, K.; Okuhara, T.; Misono, M. Active Crystal-Face of Vanadyl Pyrophosphate for Catalytic-Oxidation of *n*-Butane to Maleic-Anhydride, *Chem. Lett.*, **1992**, 1955–1958. DOI: 10.1246/cl.1992.1955
- (42) Okuhara, T.; Inumaru, K.; Misono, M. Active Crystal Face of Vanadyl Pyrophosphate for Selective Oxidation of *n*-Butane, *Catalytic Selective Oxidation*, Chapter 12, pp 156–167, Oyama, S. T., Hightower, J. W., Eds.; *ACS Symposium Series*, *523*, 1993. DOI: 10.1021/bk-1993-0523.ch012
- (43) Ohno, T.; Sarukawa, K.; Matsumura, M. Crystal Faces of Rutile and Anatase TiO<sub>2</sub> Particles and Their Roles in Photocatalytic Reactions, *New J. Chem.*, **2002**, *26*, 1167–1170. DOI: 10.1039/b202140d
- (44) Takata, T.; Jiang, J. Z.; Sakata, Y.; Nakabayashi, M.; Shibata, N.; Nandal, V.; Seki, K.; Hisatomi, T.; Domen, K. Photocatalytic Water Splitting with a Quantum Efficiency of Almost Unity, *Nature*, **2020**, *581*, 411–412. DOI: 10.1038/s41586-020-2278-9
- (45) Costa, D. G.; Rocha, A. B.; Souza, W. F.; Chiaro, S. S. X.; Leitão, A. A. Ab Initio Study of Reaction Pathways Related to Initial Steps of Thermal Decomposition of the Layered

Double Hydroxide Compounds. *J. Phys. Chem. C*, **2012**, *116*, 13679–13687. DOI:  
10.1021/jp303529y

## TOC Graphics

